Int J Appl Earth Obs Geoinformation 64 (2018) 171–180

Contents lists available at ScienceDirect

Int J Appl Earth Obs Geoinformation

journal homepage: www.elsevier.com/locate/jag

# Complex surface deformation of Akutan volcano, Alaska revealed from InSAR time series

Teng Wang[a,*], Kimberly DeGrandpre[a], Zhong Lu[a], Jeffrey T. Freymueller[b]

[a] Huffington Department of Earth Sciences, Southern Methodist University, Dallas, TX, USA
[b] Geophysical Institute, University of Alaska Fairbanks, Fairbanks, AK, USA

ARTICLE INFO

*Keywords:*
Volcano deformation
InSAR
Aleutian arc

ABSTRACT

Akutan volcano is one of the most active volcanoes in the Aleutian arc. An intense swarm of volcano-tectonic earthquakes occurred across the island in 1996. Surface deformation after the 1996 earthquake sequence has been studied using Interferometric Synthetic Aperture Radar (InSAR), yet it is hard to determine the detailed temporal behavior and spatial extent of the deformation due to decorrelation and the sparse temporal sampling of SAR data. Atmospheric delay anomalies over Akutan volcano are also strong, bringing additional technical challenges. Here we present a time series InSAR analysis from 2003 to 2016 to reveal the surface deformation in more detail. Four tracks of Envisat data acquired from 2003 to 2010 and one track of TerraSAR-X data acquired from 2010 to 2016 are processed to produce high-resolution surface deformation, with a focus on studying two transient episodes of inflation in 2008 and 2014. For the TerraSAR-X data, the atmospheric delay is estimated and removed using the common-master stacking method. These derived deformation maps show a consistently uplifting area on the northeastern flank of the volcano. From the TerraSAR-X data, we quantify the velocity of the subsidence inside the caldera to be as high as 10 mm/year, and identify another subsidence area near the ground cracks created during the 1996 swarm.

## 1. Introduction

Akutan island is located in the eastern section of the Aleutian volcanic arc, a chain of islands that extends ~2000 km along the convergent boundary where the Pacific plate subducts beneath the North American plate (Fig. 1, inset). In the west-central part of the island, a composite stratovolcano with a circular summit caldera rises ~1300 m above sea level (Fig. 1). A 240 m high, 1 km wide cinder cone is situated in the northeast quadrant of the caldera (Newhall and Dzurisin, 1988; Miller et al., 1998). Volcanic deposits, such as lava and pyroclastic flows, cover the majority of the western half of the island, but in the east, the topography becomes more complicated, The surface here includes a series of NW-SE trending lateral ridges dominated by older, relatively loose tephras and ashes (Newhall and Dzurisin, 1988; Miller et al., 1998). Akutan island has a vegetated coastline and is sparsely inhabited with a population of ~1000 people living primarily in Akutan Village, on the edge of Akutan Bay,13 km away from the summit (Fig. 1).

Akutan volcano is one of the most active volcanoes in the Aleutian arc (Lu and Dzurisin, 2014). At least 27 episodes eruptive activities have been noted since 1790. Akutan is capable of both effusive and explosive eruptions, but most of the reported eruptions included small-to-moderate explosions of VEI 2 from the intracaldera cone. In 1929, a lava flow breached the caldera rim through a gap on the northwest side and extended ~0.7 km down the northwestern flank, triggering small lahars that flowed into valleys to the north and northwest. An explosive eruption in 1948 was preceded by a seismic swarm that was felt by the people of Akutan Village and produced measurable amounts of ash deposits that reached the eastern extent of the island. The 1978 eruption ejected large incandescent bombs from the summit and produced lava flows down the volcano's north flank. The most recent eruptive activity was a series of small (VEI 1) steam and ash emissions from the summit cone from March to May of 1992. Four years later, in early March of 1996, an intense swarm of volcano-tectonic earthquakes shook the Akutan island. Immediately after this swarm began, Alaska Volcano Observatory (AVO) installed a seismometer in the city of Akutan and a network of four seismic stations on the eastern side of the island. The 1996 seismic swarm continued for several months, but seismic activity had ceased by July 1996. That July, an additional network of six permanent seismic stations was installed island-wide by AVO scientists, which was eventually increased to 15 stations in the following years (Fig. 1). Since then, more than 3000 earthquakes have

* Corresponding author. Present address: Earth Observatory of Singapore, Nanyang Technological University, Nanyang Ave, Singapore.
*E-mail address:* wang.teng@gmail.com (T. Wang).

http://dx.doi.org/10.1016/j.jag.2017.09.001
Received 6 May 2017; Received in revised form 19 August 2017; Accepted 1 September 2017
Available online 21 September 2017
0303-2434/ 

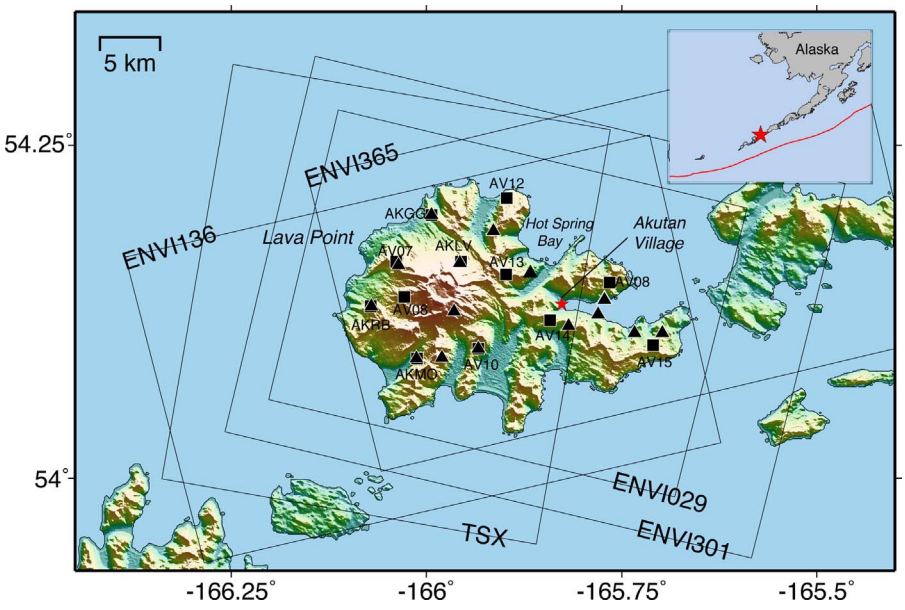


**Fig. 1.** Topography of Akutan island with GPS and seismic stations, and SAR image outlines plotted. Black squares are GPS stations; black triangles are seismic stations; rectangles represent InSAR data coverage. Inset is the location of Akutan island in the Aleutian volcanic arc, to the west of mainland Alaska.

been located in this region, but the peak of activity was March 11 and 16, 1996. The estimated cumulative seismic moment of the 1996 swarm is approximately equivalent to a magnitude 6 event, yet failed to result in an eruption (Power et al., 1996; Lu et al., 2000). However, a series of fresh ground cracks that extend discontinuously from Lava Point to the southeast side of the island, with a strike of ~N70°W were identified during field work in the summer of 1996. The most significant ground cracks appeared in a rectangular area between Lava Point and the summit, in a zone with a width of 300–500 m and total length of 3 km (Lu et al., 2005).

The surface deformation before, during, and after the 1996 seismic swarm has been studied using Synthetic Aperture Radar Interferometry (InSAR) (Lu and Dzurisin, 2014; Lu et al., 2000; Lu et al., 2005). C-band ERS and L-band JERS interferograms spanning the swarm revealed more than 60 cm of uplift in the western half of the island, but a similar amount of subsidence distributed across the eastern half can only be observed in the L-band interferograms that exhibit much higher coherence in this region. Before and after the 1996 seismic swarm, the surface deformation exhibited similar patterns, i.e. the volcano's northeast flank uplifts about 10 mm per year relative to the southwest flank (Lu et al., 2005). An interesting feature that can only be detected from interferograms acquired after the swarm is the subsidence along a system of cracks created during the swarm.

SAR images acquired by the Envisat satellite during 2004–2009 reveal that the northwest part of the island was still uplifting at a similar magnitude of 10 mm/year (Lu and Dzurisin, 2014). An inflating dike at ~6 km deep can explain the observed spatial deformation (Lu and Dzurisin, 2014). However, due to the loss of coherence and strong atmospheric delays, it is difficult to determine whether the observed deformation was due to the long-term inflation or the transient inflation that occurred between 2004 and 2009. In addition to the observed deformation on the flanks of the volcano, a persistently subsiding area inside the caldera was also discovered from Envisat interferograms, which was probably due to depressurization of a shallow hydrothermal system (Lu and Dzurisin, 2014).

InSAR is an imaging tool for mapping the spatial distribution of surface deformation, but the satellite revisit period limits temporal resolution, preventing constraints on the sequence of deformation events. Conversely, GPS data can have very high resolution in time but limited spatial coverage. Transient inflation during the first half of 2008 was detected and modeled as a simple Mogi source at shallow depth (~3.9 km) from GPS time series data (Ji and Herring, 2011). The difference between the GPS (Ji and Herring, 2011) and InSAR (Lu and Dzurisin, 2014) models motivates us to further investigate the deformation at Akutan volcano.

A recent study reveals the complex nature of Akutan island from the simultaneous inversion of the 1996–2009 seismic body and surface wave data for a more accurate velocity model and event relocations (Fig. 2) (Syracuse et al., 2015). The spatial and temporal patterns seen in the seismic tomography and relocation inversion results (Fig. 2) suggest that the surface deformation may reflect multiple mechanisms both spatially and temporally. GPS time series, in general, are sensitive in time, and can detect transient inflation signals, but are not dense enough to reveal the spatial distribution of surface deformation, making it difficult to constrain the geometry of the source. It is therefore essential to utilize spatially high-resolution InSAR data of the same period to study the source of surface deformation. Here we analyzed Envisat and TerraSAR-X InSAR data from 2002 to 2015 to reveal the complex surface deformation around Akutan volcano, improving our understanding of the episodic nature of the magma plumbing system beneath the island.

## 2. Datasets

### 2.1. InSAR datasets

We collected three descending tracks: Envisat T029 (24 images acquired from 2003 to 2010) and T301 (17 images acquired from 2003 to 2010), and one TerraSAR-X track (12 images acquired from 2011 to 2015). Three ascending tracks were also collected: Envisat T136 (12 images acquired from 2004 to 2010) and T365 (16 images acquired from 2004 to 2010) and one ALOS track (17 images acquired from 2006 to 2010) (see Fig. 1 for the cropped data coverage of the InSAR datasets, and Fig. 3 for data acquisition time and coherence distribution). The Envisat data were acquired in C-band (wavelength of 5.6 cm), the TerraSAR-X data were acquired in X-band (wavelength of 3.2 cm), and the ALOS data were acquired in L-band (wavelength of 23.6 cm). The acquisitions of the TerraSAR-X data have been carefully programmed to avoid any winter months when snow cover would result in decorrelation. Unfortunately, many of the ALOS data were acquired in winter, resulting in much lower coherence for many of the ALOS interferograms, despite the effect of a longer wavelength that usually produces higher coherence in InSAR images (e.g. (Lu and Dzurisin, 2014; Lu et al., 2005)). The extent of decorrelation in the ALOS dataset

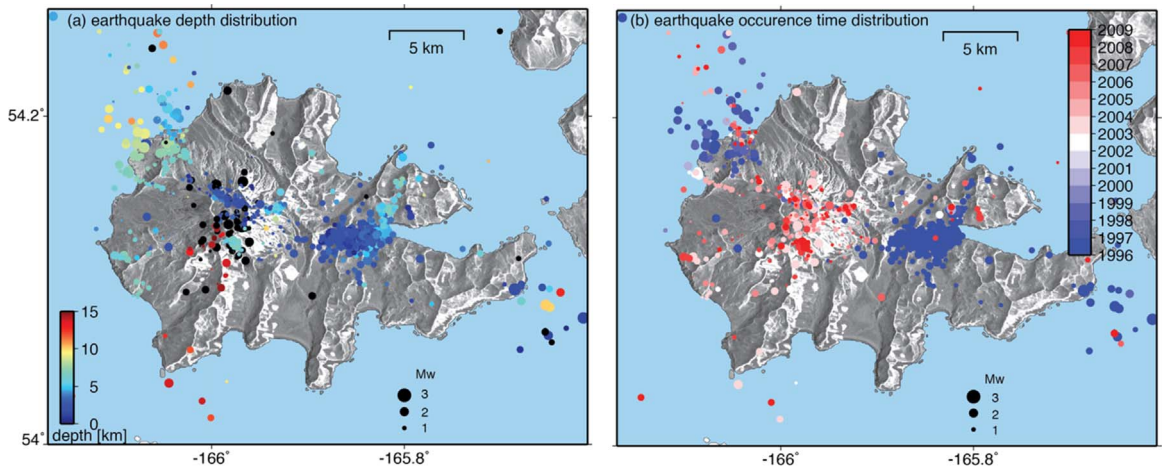


**Fig. 2.** The distribution of relocated earthquakes on Akutan island, from Syracuse et al. (2015). The magnitudes of the earthquakes in both panels are shown by the size of the circles. Event distribution is colored by depth (a), with black circles signifying earthquakes that occurred more than 15 km deep. Event distribution in time (b) is also provided with color indicating the year of the event.

rendered it unusable for our purposes and will not be presented in this study. The overall coherence of the Envisat data is much lower than the TerraSAR-X data, as a result of the relatively lower spatial resolution and longer temporal revisit period in Envisat acquisition (Fig. 3). The InSAR coherence maps also reflect the distribution of vegetation and loose volcanic material on Akutan island as the coherence is much lower in the eastern part of the island (Lu and Dzurisin, 2014).

### 2.2. GPS data

Akutan island has 16 campaign and 12 continuous GPS sites operating since 2006. Campaign GPS sites are short term occupations that require repeat visits, often occurring at intervals of a year or more. Due to this temporal limitation of data from the campaign sites only data from the 12 continuous GPS sites, publically available through UNAVCO and the Plate Boundary Observatory (PBO; http://pbo.unavo.org), are used in this study (Fig. 1). Most of the stations have continually acquired data since 2004–2005, but for some of the stations, there are data gaps in certain years.

GPS velocities reflect the summation of all velocities acting on a location, so to isolate volcanic deformation from the tectonic motion, we calculate all GPS velocities relative to site AV15, located on the far-east peninsula of the island. The assumption that AV15 is far enough from the volcano, and therefore not effected by volcanic deformation is based on previous studies that show little localized deformation in this area (e.g., (Lu and Dzurisin, 2014; Ji and Herring, 2011)). In doing so the GPS data are converted to relative velocities, and the reference frame used is no longer relevant. Here the GPS data are used to identify the timing of transient inflation signals and to calibrate the InSAR results. Based on the GPS time series, two distinct inflation episodes are observed: one is from July 1, 2007 to Jan 1, 2009 (hereafter referred to as the 2008 inflation episode), and the other from July 1, 2013 to Jan 1, 2015 (referred to here as the 2014 inflation event). More details about the GPS data and models derived from GPS time series at Akutan can be found in DeGrandpre et al. (2017).

## 3. Methods

### 3.1. InSAR processing

For each InSAR dataset, we coregistered and resampled all the images with respect to a selected master image that has the highest

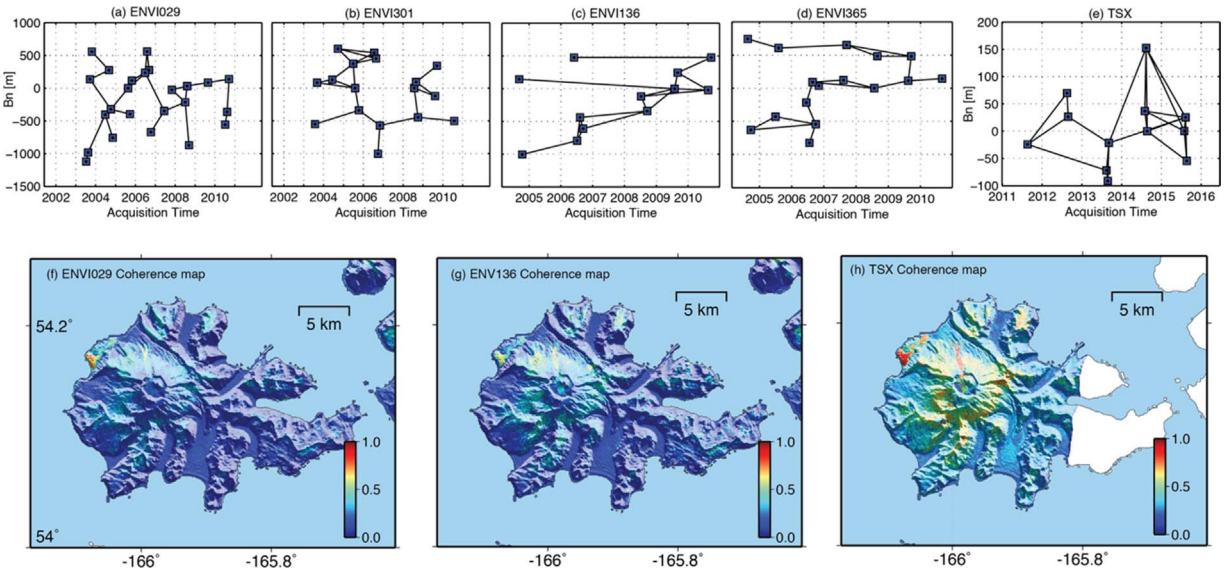


**Fig. 3.** InSAR interferogram temporal and spatial baselines are connected (a-e) for each pair of images. The averaged coherence maps for the two Envisat (ENVI) (f and g) and TerraSAR-X (TSX) (h) datasets show the relatively good coherence of TSX when compared with ENVI data. Areas of decorrelation are due to loose material or vegetation coverage.

quality index in a small-baseline coregistration strategy, which is based on the orbital information and the Digital Elevation Model (DEM) (DeGrandpre et al., 2017). We then formed a set of multilooked small-baseline interferograms to include all possible interferometric combinations. Based on the coherence maps calculated from these small-baseline interferograms, we derived a Minimum Spanning Tree (MST) to connect all *N* images using *N-1* interferograms (Wang et al., 2014) and calculated a full resolution mean coherence map based on these interferograms (Fig. 3f–h). We then identified Persistent Scatterer (PS) candidates for each dataset using given mean coherence thresholds and amplitude dispersion thresholds (0.3–0.5 for the mean coherence, and 0.2–0.45 for the amplitude dispersion, depending on different datasets). After PS candidate identification, we extracted the interferometric phases for each PS candidate from a set of small-baseline interferograms. The interferometric phases for each PS candidate were filtered by adaptively averaging the phases, weighted by the coherence, within a pre-assigned window before extraction of this phase value (Wang et al., 2014). The following procedures are point-based analysis of these PSs. We used the statistical-cost approach implemented in StaMPS to unwrap phases of sparse PSs (Perissin and Wang, 2012; Chen and Zebker, 2000). After phase unwrapping, we implemented different time series InSAR processing strategies to estimate the cumulative deformation on the island of Akutan.

### 3.2. Cumulative deformation during the 2008 inflation episode from Envisat images

It is very challenging to implement standard PS interferometry in the Aleutian Islands as the deformation rate is small (less than 15 mm/year for our case) and snow-free acquisitions are limited to summer months, from July to September. This is even more difficult when using Envisat data because of the coarse resolution and sparse temporal distribution. For these images, the PS-like method (e.g., (Hooper, 2010; Ferretti et al., 2001)) is not applicable, as interferograms with long temporal and spatial baselines are often completely decorrelated. MST-like (e.g., (Wang et al., 2014)) interferometric configuration may not be reliable either, as decorrelated interferograms have to be included in the time series inversion to keep all the images connected. The standard Small-Baseline Subset (SBAS) analysis can invert for time series from disconnected image subsets using singular value decomposition given the rank-deficient design matrix (Hooper et al., 2004). Stacking coherent interferograms is another way to estimate velocity from disconnected image subsets. However, the limitation of these methods is that they assume the deformation exhibits linear temporal behavior, which is not the case for Akutan island, as indicated by the GPS time series (e.g., (Ji and Herring, 2011)). Therefore, for the Envisat datasets, we need to consider a different interferometric combination strategy to derive the deformation due to the inflation event in early 2008.

We applied an MST plus small-baseline interferometric configuration to the Envisat data by adding coherent interferograms to the MST (Fig. 3a–d). This method allowed us to take advantage of as many interferograms as possible, while keeping all of the images connected. We then estimated the time series deformation from the small-baseline interferograms, and derived the cumulative deformation from the difference between the averaged deformation before and after 2008, where outlier images can be detected from GPS time series. The derived time series using this method was then compared with GPS time series, which have been converted to radar line-of-sight direction using the radar look vector calculated for each GPS station location (Fig. 4).

From the three GPS stations located on the uplifting portion of the island, AKLV, AV13 and AV08 (Fig. 4, and see Fig. 1 for their locations), inconsistencies and outliers become evident. These were mostly due to decorrelated interferograms, that are required to keep the time series connected. We identified such outlier images by calculating the standard deviations of the difference between the InSAR interferograms and GPS time series deformation at the location of each GPS site. The images with large standard deviations were removed. We calculated the average deformation in the remaining time series maps derived from images acquired from 2005 to 2008 and images from 2009 to 2010 separately to further reduce the temporally uncorrelated noises. Then we differenced the two averaged deformation maps to isolate the deformation that occurred during the 2008 inflation from any long-term signal. In order to improve the signal-to-noise ratio (SNR) and to reduce isolated PS outliers, we uniformly distributed 300-by–300 m grids on the island and selected the median value among the PSs within each grid to represent the deformation of that grid (Fig. 5). Here, we only show the radar line of sight (LOS) displacement derived from the descending track T301 and the ascending track T365 as they have relatively higher SNR than the other two tracks. For the purpose of modeling, we mask out the caldera area that is rapidly subsiding, most likely from shallow surficial processes related to hydrothermal changes (Lu and Dzurisin, 2014).

### 3.3. Time series analysis of the TerraSAR-X data

The TerraSAR-X data exhibit good coherence for most of the interferograms (Fig. 3h). Inspecting the high-resolution TerraSAR-X InSAR images reveals very complicated fringe patterns, some of which are likely not related to actual surface deformation. We excluded the possibility of large topographic errors as a source for the observed fringes because interferograms with larger perpendicular baselines do not display larger phase changes. All the interferograms showing complicated fringe patterns are associated with specific images, suggesting that the origin of these fringe patterns is the Atmospheric Phase Screen (APS), which represents the stratified atmospheric conditions at the time of acquisition. As shown in Fig. 6, similar features appear in the interferograms created using the image acquired on Aug. 23, 2014.

In order to improve the time series analysis and for the benefit of future studies concerning the APS distribution due to the extreme weather conditions in this region, we implemented the common-master stacking strategy to the TerraSAR-X dataset to extract the APS from a full connection of interferograms (Berardino et al., 2002). The basic idea is to form and sum all the possible interferograms with the same master to obtain the APS of each individual image, instead of each interferogram. During the stacking, the APS from the master image has been propagated through all the interferogram, while the APS from other images have been eliminated due to the uncorrelation of APS in time.

We generated a full connection of 12 TerraSAR-X images, i.e. 66 interferograms to estimate the APS. The APS signal is relatively smooth in space, so to facilitate phase unwrapping we downsampled the PSs by averaging the phases within 50 m-by–50 m grid cells for the imaged area. The PSs in the decorrelated eastern region of the island and the PSs showing strong localized subsidence within the caldera are masked out. The deformation at these locations is assumed to be related to localized and shallow hydrothermal processes and not a result of changes in the magma source parameters. We unwrapped the downsampled phases to estimate LOS ground-to-sensor changes in distance and then averaged these LOS changes for each image (Berardino et al., 2002). We also applied the low-pass filtering to the APS series to extract the time dependent signal which was then removed. We then calculated the standard deviation of the APS associated with each image and removed the APS showing the largest standard deviation from all the related interferograms. We iteratively implemented this procedure until the derived APS with the largest standard deviation was smaller than a given threshold. To retrieve the APS estimate for all of the PSs we applied Kriging interpolation to the downsampled locations of the APS in each image (e.g., (Hooper, 2010)). We selected 22 of these interferograms with relatively high coherence and few unwrapping errors for inversion to construct a time series of surface deformation. The interpolated APS can finally be removed from the inverted time series of deformation for each PS, improving the time-dependent signal, i.e.

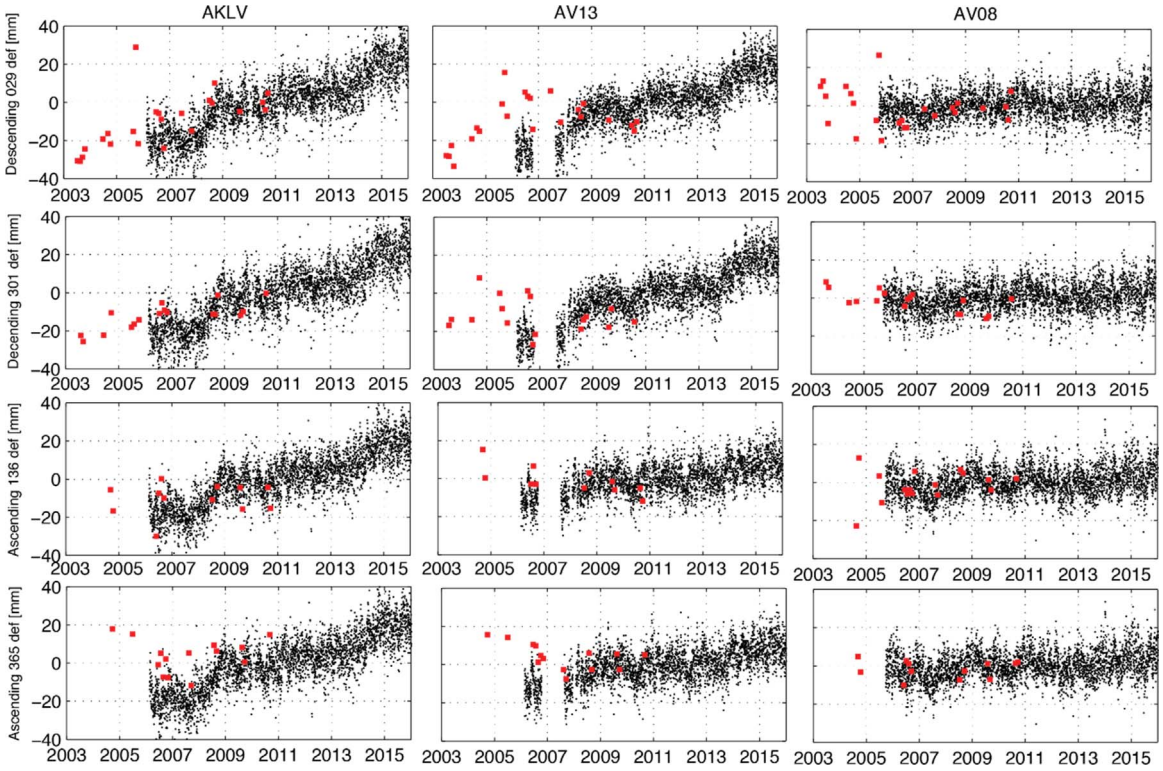


**Fig. 4.** Comparison of GPS and InSAR time series from Envisat data at GPS station AKLV (first column), AV13 (second column), and AV08 (third column). InSAR time series are represented as red squares, and compared with GPS time series, which are represented as small black dots.

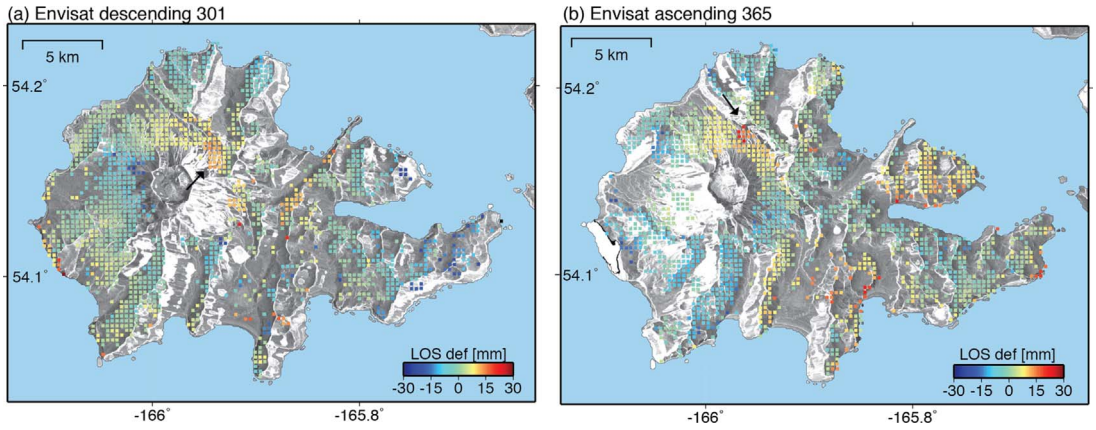


**Fig. 5.** Downsampled LOS deformation spanning the year 2008 from two of the Envisat datasets, descending track 301 (a), and ascending track 365 (b). Back arrows indicate locations of the peak deformation on the northeast flank.

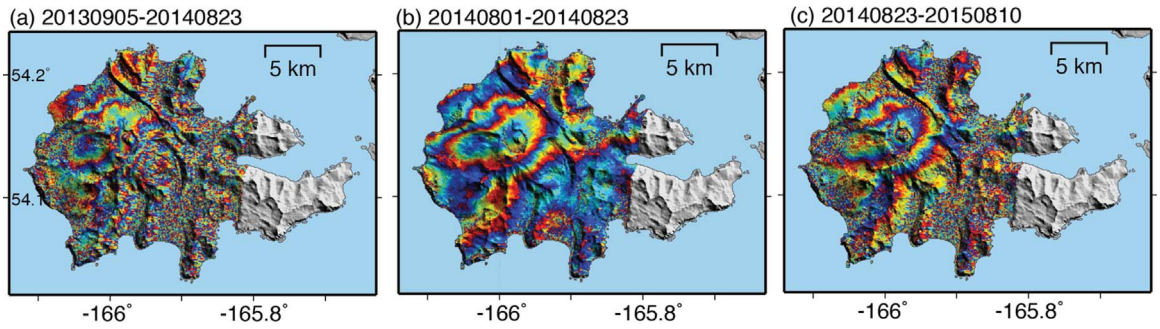


**Fig. 6.** Atmospheric phase screen (APS) associated with TerraSAR-X image acquired on Aug. 23, 2014. These interferograms (a–c), created using the same image acquired on Aug. 23, 2014, exhibit similar features regardless of temporal duration.

deformation of the Akutan island from 2011 to 2015.

## 4. Results

### 4.1. Uplift of the north/northeast flank from InSAR data

For the Envisat datasets that span the 2008 inflation, results from both the descending and ascending tracks generally show a deforming area on the northeast flank of the volcano, with the ground moving toward the satellite, indicating that the main component of the deformation was uplift (Fig. 5). However, peak deformation in each of the datasets is located in a different area on the flank of the volcano. This is most likely because the horizontal motion exhibits opposite signs when projected into the ascending and descending LOS directions. For the descending track, the eastward motion of the east flank and the uplift both shortening the sensor-to-target distance, while for the ascending track, the east motion of the east flank and the uplift have opposite signs when projected to the LOS direction, shifting the peak of LOS deformation westwards for the ascending track. This is consistent with the GPS vectors, which show the divergent characteristics of the horizontal motion (e.g., (Ji and Herring, 2011)). Note that the SNR seems less than the results from the stacking result derived from all the coherent interferograms (e.g., (Lu and Dzurisin, 2014)), because we did not include any interferograms created using images acquired before 2006. However, by doing this, we can ensure that the derived cumulate deformation originates only from the 2008 inflation event as detected from the GPS time series.

The TerraSAR-X data reveal a similarly deformed area, but have a more dense spatial distribution of data points than the Envisat dataset (Figs. 7 and 8) so that the extent of the observed uplifting area can be clearly identified. The time series analysis using TerraSAR-X data also allows us to recognize that there was a transient period of uplift that started in the beginning of 2014 and ended before the end of 2015, which is consistent with GPS time series data (Fig. 8b and c). The cumulative deformation calculated for these 2008 and 2014 events reveal similar magnitudes and spatial patterns, suggesting that the mechanism responsible for the deformation during these two periods might be the same and exhibiting episodic behavior.

### 4.2. Modeling the uplifting flank

The measured surface displacements from Envisat and TerraSAR-X data were inverted for both a Mogi (Mogi, 1958) inflation point source inflation (Table 1) and Okada (1985) dike expansion model (Table 2). The data were inverted independently to allow for comparisons between data quality and results. For each dataset the residual sum of squares (RSS) for 1000 Monte Carlo simulations were evaluated using the “trust-region-reflexive” non-linear least squares inversion Mogi (1958). Unfortunately, given the noisy InSAR data, it is difficult to obtain consistent models from the surface displacement derived from these different datasets. This is particularly true for the Envisat data because PS points are more sparse than the TerraSAR-X data and due to the large number of outliers in these smaller datasets the stability of the model parameters is especially reduced. The best fit models for Envisat datasets are presented in Tables 1 and 2, but are not discussed further because they are not considered to be significant results.

The surface deformation predicted by both a Mogi point source and an Okada dislocation plane can largely represent the observed deformation in TerraSAR-X data. The geometric parameters of the best fit Okada plane defined here (Table 2) are similar to the dike described by Lu et al. (2005) and align with observed seismic trends. However, the detailed slip distribution cannot be resolved because of the many outliers that are a result from decorrelation and localized APS anomalies. The spatial pattern of the residuals for each of the models are very similar (Fig. 7, right column), making it difficult to visually determine the dominant mechanism creating the observed deformation. A clear discontinuity between uplift and subsidence on the east flank of the volcano that is aligned with an anomalous area of subsidence on the northwest flank (Figs. 7 and 8) is observed in the residual pattern for both models. Because these features cannot be resolved with either of the source models tested here we attribute this deformation to shallow surficial processes.

While it is visually difficult to identify the best fit model, the RSS value for the Mogi model (2.26, Table 1) is clearly a better fit than the Okada model (23.32, Table 2) for the TerraSAR-X data spanning the 2014 inflation event. This is considered significant because the Okada model has more degrees of freedom (8 parameters) with which to fit the data than the Mogi model (4 parameters). A best fit Mogi model of a spherical magma chamber at a depth of 2.3 km (Table 1) below the

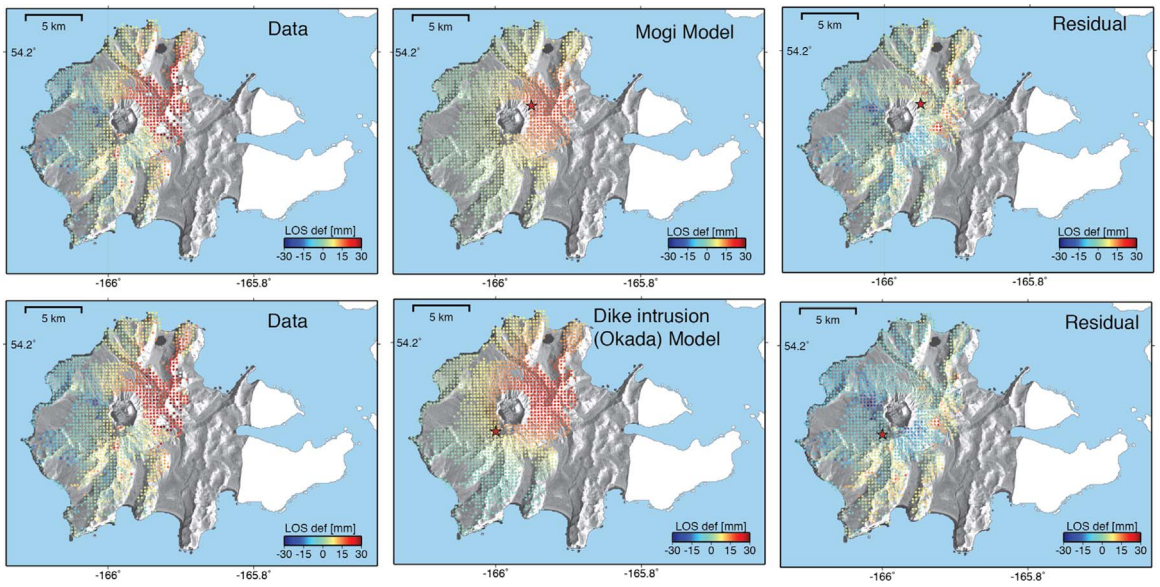


**Fig. 7.** Observed, best fit magma source models, and residuals of the downsampled LOS deformation from TerraSAR-X data. The top row are the Data/Model/Residual images resulting from the best fit spherical magma chamber (Mogi point source model). The red star indicates the center of this spherical source. The bottom row are the Data/Model/Residual images for the best fitting results of an opening dike in the elastic half space (Okada dislocation plane model). The red star indicates the center of the top of this plane.

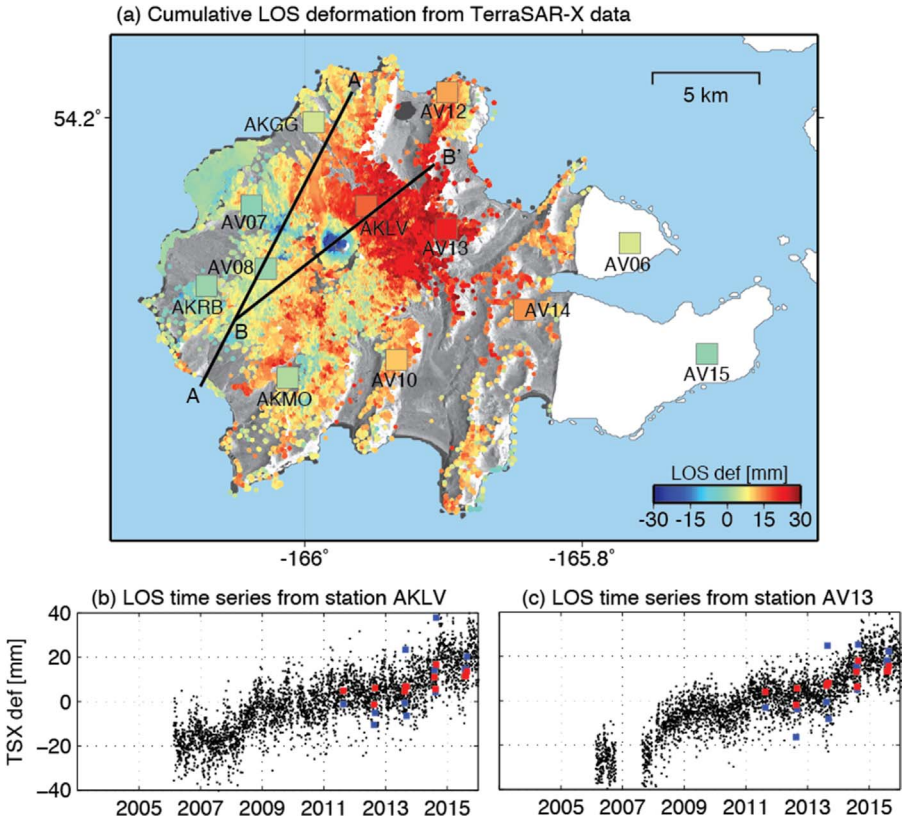


**Fig. 8.** Surface deformation from the Persistent Scatterer analysis of TerraSAR-X data. The cumulative deformation in the radar LOS direction is compared with GPS data (big squares) that is also projected into the radar LOS (a). Two deformation profiles, across the subsidence feature on the west flank (A-A') and across the caldera (B-B') are shown in Fig. 9. The time series deformation from InSAR and GPS are compared at station AKLV (b) and AV13 (c). Red and blue squares represent time series deformation from TerraSAR-X data with and without APS correction, respectively.

**Table 1**
Best fit Mogi model parameters for each set of surface deformation data.

| Data | Depth (km) | Longitude (deg. E) | Latitude (deg. N) | Volume ($km^3$) | RSS |
|---|---|---|---|---|---|
| Envi 301 | 1.26 | −165.717 | 54.187 | 0.0131 | 35.07 |
| Envi 365 | 3.59 | −165.737 | 54.108 | 0.0084 | 37.39 |
| TSX | 2.255 | −165.838 | 54.156 | 0.011 | 2.26 |

north flank of the volcano (Fig. 7) may be a better fit to the TerraSAR-X data than the Okada model, but it is not considered to be realistic because of the uncertainty and noise associated with the InSAR PSs.

We have also tried to model both the InSAR and GPS data together. However, due to the localized deformation and the low SNRs of the InSAR PSs, we have to significantly downweight the InSAR data for the model parameters to converge. This downweighting essentially creates model inversions that are based on the GPS data alone. Quality is significantly improved and the number of measurements is increased in the TerraSAR-X dataset when compared with the Envisat datasets, but the TerraSAR-X data is limited to a descending orbit and ascending data is unavailable. With only one LOS direction to provide constraints it is difficult to resolve tradeoffs between model parameters. Three component displacement time series provided by GPS data are thus essential in determining reliable model parameters. Therefore, in the following sections, we will focus on the interpretation of the observed surface deformation related to shallow processes and not on the results of the model inversions. Readers who are more interested in understanding the deeper magma source processes revealed from modeling GPS data can refer to DeGrandpre et al. (2017) for more details.

### 4.3. Localized areas of subsidence from TerraSAR-X InSAR time series

When the pixel spacing in a SAR image is large (~10–20 m), as is the case with Envisat data, many scatterers in the resolution cell can reflect the microwave back to the satellite, reducing the interferogram coherence. Conversely, high-resolution data, such as the images from the TerraSAR-X satellite, have smaller pixel dimensions and can better preserve coherence because there are fewer scatterers within each pixel. The smaller pixel size in high-resolution data also allows for more detailed mapping of smaller deformation features and makes it is possible to derive deformation time series for these areas of localized motion.

In addition to the obvious uplift occurring on the northern flank of the volcano, two isolated areas of subsidence are identified from the time series analysis of the TerraSAR-X data. One is a rectangular region of the western flank of the volcano (Fig. 9a and b) and the other is an incomplete circular feature inside the caldera (Fig. 9a and c). Although these two areas of subsidence were also observed by stacking Envisat summer interferograms, quantifying the deformation from this mid-resolution SAR data was challenging (Lu and Dzurisin, 2014). We were,

**Table 2**
Best fit Okada model parameters for each set of surface deformation data

| Data | Length (km) | Width (km) | Depth (km) | Dip (deg.) | Strike (deg.) | Longitude (deg. E) | Latitude (deg. N) | Strike-slip (mm) | Dip-slip (mm) | Opening (mm) | RSS |
|---|---|---|---|---|---|---|---|---|---|---|---|
| Envi 301 | 15.00 | 2.00 | 2.58 | -89.18 | 121.23 | −165.90 | 54.13 | 432.73 | 139.10 | 27.77 | 29.00 |
| Envi 365 | 7.76 | 7.17 | 0 | -84.03 | 112.52 | −165.90 | 54.13 | 253.22 | −73.78 | 10.62 | 31.61 |
| TSX | 8.90 | 8.22 | 0.66 | -72.31 | 132.76 | −166.00 | 54.16 | −134.5 | −74.90 | −51.50 | 23.32 |

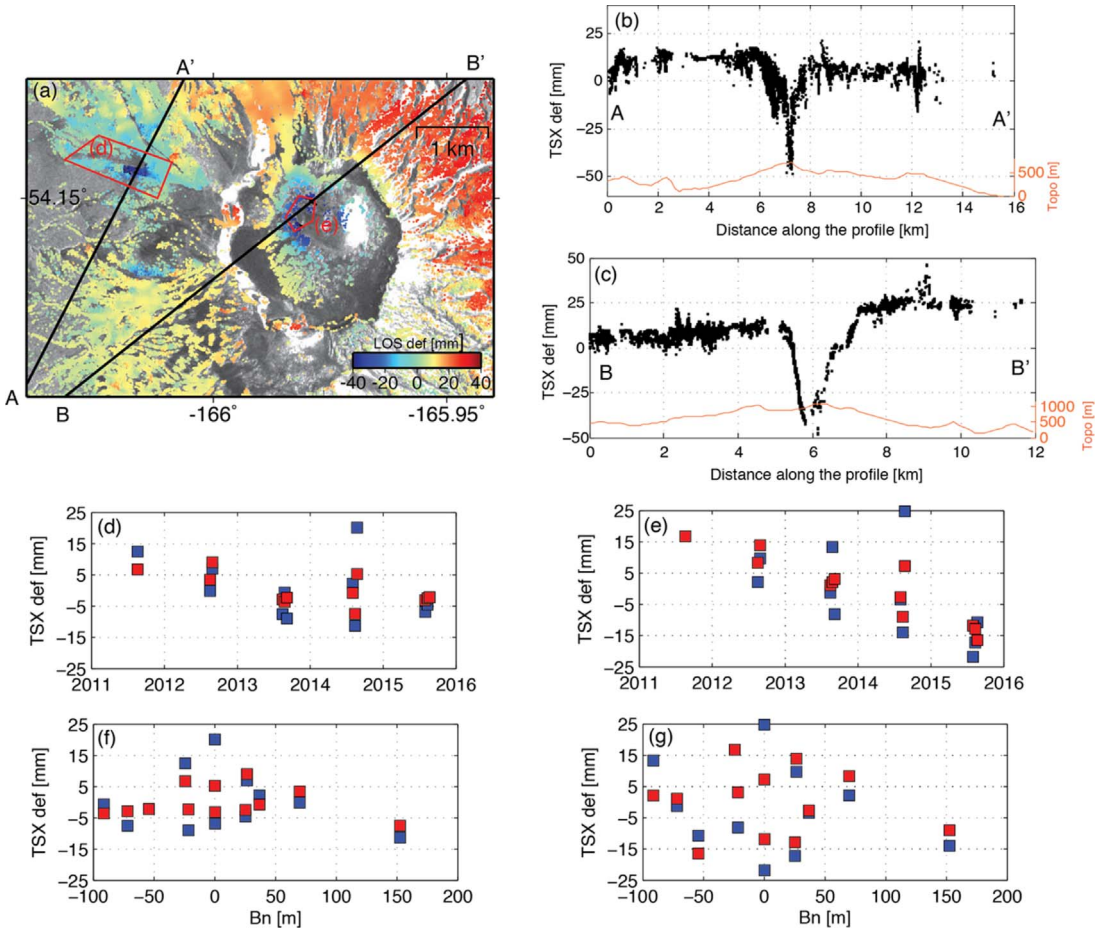


**Fig. 9.** Detailed surface deformation near the summit area derived from TerraSAR-X data. TerraSAR-X LOS deformation along the two profiles A-A' and B-B' (Fig. 8a) are plotted (b and c, respectively). InSAR time series deformation (d and e) is calculated by averaging the deformation within the two corresponding red polygons in (a), which represent a possible small graben structure (d) and a potential geothermal field within the caldera (e). Deformation with respect to perpendicular baseline (Bn) is also plotted (f and g) to demonstrate that there is very little topographic error in the time series analysis. Red and blue squares represent results with and without APS correction, respectively.

however, able to explore the spatial and temporal behavior of these localized subsidence features from the many coherent, high-resolution TerraSAR-X interferograms. The deformation time series with and without APS correction are plotted by averaging the PSs located in the subsiding areas (Fig. 9a, d, and e). In order to evaluate the possibility that the inclusion of topographic errors associated with the DEM is influencing our time series analysis, we also plotted the derived LOS displacement with the perpendicular (normal) baselines of the interferograms (Fig. 9f and g). The areas of subsidence clearly exhibit time dependent behavior after the APS correction (Fig. 9d and e), yet no correlation with perpendicular baseline is obvious (Fig. 9f and g), suggesting that the observed signals are mostly due to surface deformation rather than topographic errors.

The extensive zone of ground cracks on the western flank between Lava Point and the summit, identified by AVO scientists following the 1996 seismic swarm, exhibited initial subsidence of 30–80 cm (Lu et al., 2000; Lu et al., 2005). Ongoing measurements using SAR images acquired from 1997 to 2000 revealed that the maximum rate of subsidence (~20 mm/year) occurred during 1996–1997, and then progressively reduced to about 10 mm/year (Lu et al., 2005). Because of the dense availability and small pixel size of PSs in the TerraSAR-X images, we are able to define a rectangular, graben-like area of subsidence with a strike of ~N70°W (Figs. 8 a and 9 a), consistent with the field observations from 1996. Our analysis of the TerraSAR-X data indicates that at this feature there is ongoing subsidence of ~10 mm/year (Fig. 9d), similar to the stable trend estimated in previous studies (Lu et al., 2005), potentially signifying a constant rate of subsidence from 1997 to 2014. While the rate of subsidence at this feature remains constant in our data from 2011–2014, there is an apparent change that coincides with the initiation of the 2014 inflation event defined from the GPS time series. At this time, in early 2014, the observed deformation is significantly reduced nearly to zero and remains that way until the middle of 2015. The reason for such a deceleration is unclear, but we suspect the uplift from a deep source might negate the subsidence of the shallow graben structure, resulting in an overall trend of 0 mm/yr for this area during the inflation event.

We also discovered a bowl-shaped subsidence area inside the caldera floor in the TerraSAR-X interferograms (Fig. 9a). The preserved coherence excludes the possibility of any physical changes on the surface, such as loss of ice or snow, as the cause for this observed motion. The magnitude of this subsidence is approximately one fringe per year in the X-band interferograms, indicating a LOS velocity of ~15 mm/year. A LOS displacement profile through the caldera from south to north, derived from our PS analysis, clearly displays a peak in subsidence, centered on this circular feature, that is in stark contrast to the gradual uplift observed in the north (Fig. 9c). This sharp, localized deformation pattern implies that the source of the subsidence is very shallow. After the APS correction, this inter-caldera subsidence exhibits a very clean, linear trend with a velocity of about 10 mm/year. The linear rate of deformation supports the conclusion of Lu and Dzurisin (2014), that the subsidence should be attributed to fumarole activity on the caldera floor that provides continuous depressurization of a shallow hydrothermal system. The continued subsidence suggests that degassing of this hydrothermal system is ongoing. This degassing could be

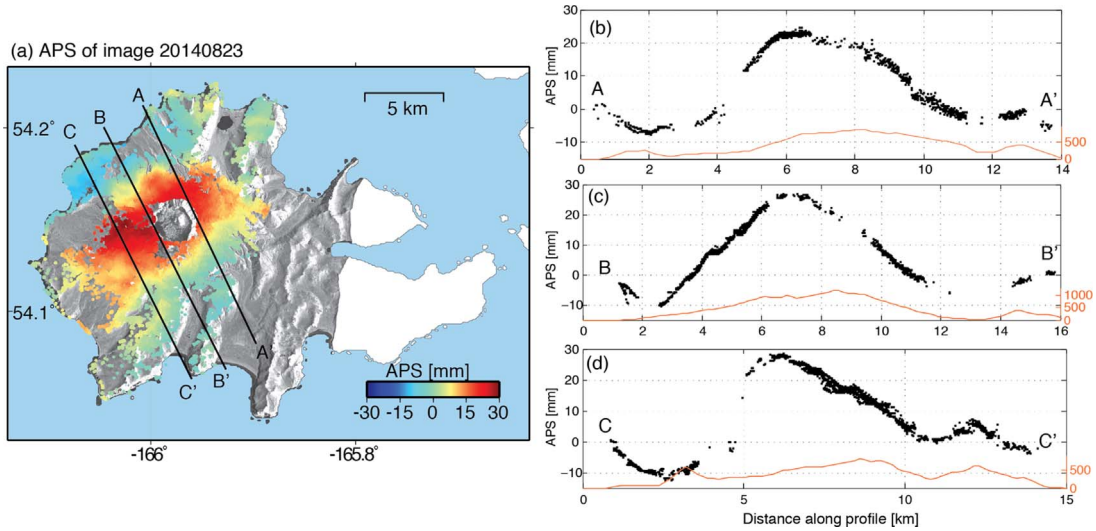


**Fig. 10.** The APS of a TerraSAR-X image acquired on Aug. 23, 2014. The APS derived using common-master stacking (a) shows correlation with topography from three parallel profiles (b–d).

related to the cooling of a shallow storage of magma interpreted in multiple geophysical datasets, including the seismic models of Syracuse et al. (2015), the GPS analysis in DeGrandpre et al. (2017) and now the TerraSAR-X data presented here.

## 5. Discussion

### 5.1. Episodic inflation at Akutan volcano

Although most of the seismicity of the 1996 earthquake swarm occurred on the eastern half of Akutan island, the western part of the island accommodated most of the surface deformation, including 60 cm of uplift at the northern flank of the volcano and the opening of the small graben on the northwest flank (Lu et al., 2000; Lu et al., 2005). Our analysis of the InSAR time series data presented here indicates that the surface deformation during the 2008 and 2014 inflation events exhibit similar patterns to that of the 1996 swarm. From our InSAR observations, we are disposed to the explanation that the inflation at Akutan island is episodic, causing the 1996 earthquake swarm as well as the 2008 and 2014 transient signals detected in the GPS time series. During the 1996 swarm, the magma cracked the upper crust of the west part of the island, intruded as a dike beneath the volcano, and formed the graben structure in the west flank when it failed to erupt and began to cool and contract. Since then, several smaller episodes of inflation have occurred, in 2008 and 2014, producing the regional uplift of the north flank, as we observed from InSAR data discussed here.

### 5.2. The complementary use of InSAR and GPS data for observing volcanic deformation

Continuous GPS stations installed across Akutan island, provided deformation time series with high temporal resolution so that we are able to detect the transient inflation signals in 2008 and 2014 (e.g. (Ji and Herring, 2011)). GPS data can also provide accurate, reliable, and three dimensional geodetic measurements, that can be inverted for magma source model parameters as in DeGrandpre et al. (2017). However, installing and maintaining GPS stations is extremely difficult in the Aleutian Arc, and Akutan island is a rare case where a dense, functioning GPS network exists. There do remain spatial limitations to GPS data and even with a dense GPS network on a small island, the data are still ill-suited for capturing localized deformation features. The small graben structure located on the western flank of the volcano, which is important for implications related to the geometry of the dike intrusion, would only be detected if a GPS station was installed directly on the feature. It is also difficult to securely install GPS stations within the unstable and active caldera to detect the long-term subsidence due to the geothermal activities.

The use of InSAR data in conjunction with GPS time series advances our understanding of volcanic deformation at Akutan volcano. Due to heavy snow cover during the winter months, only year long, summer-to-summer interferograms are useable, seriously reducing the temporal resolution of InSAR data that is limited even under ideal conditions, and making it many orders of magnitude lower than that of continuous GPS data. It is therefore, difficult to detect transient temporal signals from InSAR data, but the spatial resolution and coverage provides better definition of deformation patterns and features that can be both large and small, without the need for regular installation and maintenance of ground based stations. The complementary information obtained from GPS and InSAR data is essential to the study of temporally and spatially complicated deformation. At Akutan volcano, the temporal resolution of the GPS data is used to create magma storage models through time that result in spatially extent deformation patterns, while the complementary spatial coverage of InSAR data can provide geometric details of surface deformation as well as smaller scale surficial effects that go unnoticed by both GPS and the associated deformation models.

### 5.3. Atmospheric phase screen in SAR images at volcanic islands

The APS estimated from the TerraSAR-X data allows us to discuss the spatial distribution of water vapor, which exhibits some interesting features, particularly in images acquired in the middle of August (Fig. 6 and 10a). The APS distribution of these images generally shows a smooth phase distribution across the western and eastern edges of the island, with an abrupt change often occurring at the summit that transitions to a pattern of rapid and sharp phase changes (e.g. Fig. 10). It seems that there exists a correlation between the APS and topography, but it is not a simple linear relationship (profiles in Fig. 10a–d). Similar fringe patterns from TerraSAR-X interferograms have also been observed at Cleveland volcano and other nearby islands in this region (Wang et al., 2015). This effect is probably due to the complicated interaction between water vapor, the variation in topography, and the regional wind dynamics. In other words, the atmospheric conditions around Aleutian Islands are likely to be non-hydrostatic and the non-linear relationships with topography observed at Akutan island are the results of seasonally varying atmospheric conditions.

From our observed APS distribution, we infer the water vapor

evaporating from the sea surrounding Akutan island is blown eastward by the predominant winds, where it is pushed up the west flank of the volcano, and finally accumulates at the summit. The dynamic variability coupled with high water contents result in sharp changes in the APS as vapor is blown into the flank of the volcano. At the summit, decreasing temperatures and an increase in vapor content with altitude causes the water vapor to precipitate and fall on the leeward (eastern) flank of the volcano. The water content of this air mass is decreased significantly by this process, and with decreasing wind intensity the gradual changes in the APS trend begin to have more correlation with the topography on the east half of the island. This explains why we cannot fit the APS using a simple linear relation to topography, as the atmospheric conditions on the windward side of the volcano are completely different from the leeward side. Similar atmospheric patterns have been observed not only in the Aleutian region (e.g. (Wang et al., 2015)), but also the along the Cascade volcanic arc (Parker et al., 2015). Although modeling the derived APS is beyond the scope of this study, it is an interesting way to observe that the distribution of water vapor on a volcanic island is related to wind direction.

## 6. Conclusions

SAR images acquired from Envisat and TerraSAR-X data have been analyzed using time series InSAR techniques to focus on two episodic transient inflation events in 2008 and 2014. The APSs from TerraSAR-X data have been largely eliminated using iterations of the common-master stacking technique, allowing temporal behavior of not only the large uplifting signal on the north flank but also the localized subsidence associated with surface cracks on the west flank of the volcano and geothermal processes inside the caldera. While the Envisat images proved to be too decorrelated to use for modeling purposes, the TerraSAR-X data revealed that the subtle subsidence structures on the western flank follow the linear trend of the dike proposed in previous seismic and InSAR studies (Lu et al., 2000; Lu et al., 2005; Syracuse et al., 2015). Although we have confirmed that there is a complicated plumbing system beneath Akutan volcano in the Aleutian Islands, it is a challenge to use InSAR PS data to model large, deep sources that require specific temporal delineations to properly identify episodic events at volcanoes. Nevertheless, the use of InSAR data around Akutan volcano has led to a better understanding of the complex spatial and temporal relationships between surface displacement produced by the magma storage systems at depth, as well as the surficial processes that result in smaller, localized deformation patterns.

## Author contributions

All of the authors participated in editing and reviewing the manuscript. T. Wang processed and analyzed the SAR data and drafted the initial manuscript, K. Degrandpre modeled the deformation data.

### *Conflicts of interest*

The authors declare no conflict of interest.

## Acknowledgements

Envisat data are copyrighted by the European space Agency (ESA), ALOS-1 SAR data by JAXA/METI, and TerraSAR-X data by German Aerospace Agency (DLR).This research was financially supported NASA Earth and Surface Interior Program (NNX14AQ95G), NASA Earth and Space Science Fellowship (NNX16AO26H), and the Shuler-Foscue Endowment at Southern Methodist University.

## References

Berardino, P., Fornaro, G., Lanari, R., Sansosti, E., 2002. A new algorithm for surface deformation monitoring based on small baseline differential SAR interferograms. IEEE Trans. Geosci. Remote Sens. 40, 2375–2383.
Chen, C.W., Zebker, H.A., 2000. Network approaches to two-dimensional phase unwrapping: intractability and two new algorithms. JOSA A 17 (3), 401–414.
DeGrandpre, K., Wang, T., Lu, Z., Freymueller, J., 2017. Episodic inflation and complex surface deformation of Akutan volcano, Alaska revealed from GPS time-series. J. Volcanol. Geotherm. Res submitted.
Ferretti, A., Prati, C., Rocca, F., 2001. Permanent scatterers in SAR interferometry. IEEE Trans. Geosci. Remote Sens. 39, 8–20 9.
Hooper, A., Zebker, H., Segall, P., Kampes, B., 2004. ANew method for measuring deformation on volcanoes and other natural terrains using InSAR persistent scatterers. Geophys. Res. Lett. 31.
Hooper, A., 2010. A statistical-cost approach to unwrapping the phase of insar time series. Proceeding of International Workshop on Fringe.
Ji, K., Herring, T., 2011. Transient Signal Detection Using GPS. measurements: transient inflation at Akutan Volcano, Alaska, during early 2008. Geophys. Res. Lett. 38.
Lu, Z., Dzurisin, D., 2014. InSAR Imaging of Aleutian Volcanoes: Monitoring a Volcanic Arc from Space. Springer.
Lu, Z., Wicks, C., Power, J.A., 2000. Ground Deformation Associated with the march 1996 earthquake Swarm at Akutan Volcano, Alaska, Revealed by Satellite Radar Interferometry. J. Geophys. Res. 105, B9.
Lu, Z., Wicks Jr, C., Kwoun, O., Power, J., Dzurisin, D., 2005. Surface Deformation Associated with the march 1996 earthquake swarm at Akutan Island, Alaska,R evealed by C-Band ERS and L-Band JERS Radar Interferometry. Can. J. Remote Sens. 31, 7–20.
Miller, T.P., McGimsey, R.G., Richter, D.H., Riehle, J.R., Nye, C.J., Yount, M.E., Dumoulin, J.A., 1998. Catalog of the Historically Active Volcanoes of Alaska. U.S. Geological Survey Open-File Report; U.S. Government Printing Office, Washington, DC USA.
Mogi, K., 1958. Relations Between the Eruptions of Various Volcanoes and the Deformations of the Ground Surface Around Them; Bulletin of the Earthquake Research Institute. University of Tokyo: Tokyo, Japan, pp. 99–134.
Newhall, C.G., Dzurisin, D., 1988. Historical Unrest at the Large Calderas of the World. Department of the Interior, US Geological Survey.
Okada, Y., 1985. Surface deformation due to shear and tensile faults in a half-space. Bull. Seismol, Soc. Am. 75 (4), 1135–1154.
Parker, Biggs, Walters, Ebmeier, 2015. Systematic assessment of atmospheric uncertainties for InSAR data at volcanic arcs using large-scale atmospheric models: application to the Cascade volcanoes, United States. Remote Sens. Environ. 170, 102–114.
Perissin, D., Wang, T., 2012. Repeat-pass SAR interferometry with Partially Coherent Targets. IEEE Trans. Geosci. Remote Sens. 50, 271280.
Power, J.A., Paskievitch, J.F., Richter, D.H., McGimsey, R.G., Stelling, P., Jolly, A.D., Fletcher, H.J., 1996. seismicity and ground deformation at Akutan Volcano. Amer. Geophys. Union Trans. 77, F514.
Syracuse, E.M., Maceira, M., Zhang, H., Thurber, C.H., 2015. Seismicity and structure of Akutan and Makushin Volcanoes, Alaska, using joint body and surface wave tomography. J. Geophys. Res. Solid Earth. http://dx.doi.org/10.1002/2014JB011616.
Wang, T., Jonsson, S., Hanssen, R., 2014. Improved SAR image coregistration using Pixel-offset Series. IEEE Geosci. Remote Sens. Lett. 11, 1465–1469.
Wang, T., Poland, M., Lu, Z., 2015. Dome growth at mount Cleveland, Aleutian Arc, Quantified by time series TerraSAR-X imagery. Geophys. Res. Lett. 42 (10) 10,614–10,621.